Phase transitions in bismuth-modified silver niobate ceramics for high power energy storage

Ye Tian,[1,2] Li Jin,[1] Hangfeng Zhang,[3] Zhuo Xu,[1] Xiaoyong Wei,[1*] Giuseppe Viola,[2,4]

Isaac Abrahams,[3] Haixue Yan[2*]

[1]*Electronic Materials Research Laboratory, Key Laboratory of the Ministry of Education & International Center for Dielectric Research, Xi'an Jiaotong University, Xian 710049, China*

[2]*School of Engineering and Materials Science, Queen Mary University of London, Mile End Road, London E1 4NS, United Kingdom*

[3]*School of Biological and Chemical Sciences, Queen Mary University of London, Mile End Road, London E1 4NS, United Kingdom*

[4]*Department of Applied Science and Technology, Institute of Materials Physics and Engineering, Corso Duca degli Abruzzi 24, 10129 Torino, Italy*

Corresponding Authors*

E-mail: wdy@mail.xjtu.edu.cn and h.x.yan@mail.qmul.ac.uk

Abstract

Ceramics of composition $Ag_{1-3x}Bi_xNbO_3$ ($0.005 \leq x \leq 0.040$) were prepared by solid state methods and their structure and electrical behavior were characterized with a view to their potential use as high power energy storage materials. All compositions exhibited an average orthorhombic non-polar structure. The low temperature phase transitions $M_1 \leftrightarrow M_2$ and $M_2 \leftrightarrow M_3$ and the freezing temperature T_f found in $AgNbO_3$ are increasingly shifted to lower temperatures with increasing x-value. Similarly to $AgNbO_3$, the structure of the M_2 phase above T_f is antiferroelectric. In the M_2 phase, below T_f it is proposed that the structure possesses local polar regions, which can expand during electrical loading within an average non-polar antiferroelectric matrix. The polar domains found in the M_1 phase of $AgNbO_3$ diminish with increasing bismuth content, as confirmed by the suppression of domain switching peaks in the current-polarization-electric field hysteresis loops. The antiferroelectric to ferroelectric electric field-induced transformation is progressively hindered, as the structure evolves towards long-range antiferroelectric order with increasing bismuth content. Moreover, up to a certain substitution level, bismuth addition is seen to enhance energy storage properties compared to unsubstituted $AgNbO_3$, with a high energy storage density of 2.6 J cm^{-3} and high energy efficiency of 0.86 achieved. These values make these materials amongst the best performing energy storage lead-free ceramics currently known.

Key words: dielectric, energy storage, lead-free, ferroelectrics, antiferroelectrics, $AgNbO_3$

1. Introduction

Growing demand for high-power density energy storage devices for use in portable electronics, electrical vehicles *etc*. has led to research into new dielectric energy storage materials that exhibit high efficiency. The high breakdown strength and energy density of dielectric polymers have allowed for their use in capacitors for high-power energy storage. However, polymer capacitors are limited by their application temperature range. Compared to polymers, dielectric ceramics have superior thermal properties, allowing for a wider operational temperature range. For energy storage applications, ferroelectric ceramics with high saturation polarization, low remnant polarization and high dielectric breakdown strength (E_b) are required.[1-3] The most utilized ferroelectrics are based on lead containing oxides,[4,5] but due to concerns over the toxicity of lead, there is a drive to develop Pb-free ferroelectric (FE) ceramics for many applications, including dielectric energy storage[6-10].

Silver niobate $AgNbO_3$ is a candidate material for potential application in energy storage devices. However, despite its high energy density of 2.1 J cm^{-3}, it exhibits low energy efficiency, with a relatively large hysteresis observed in ferroelectric hysteresis loops at high field.[11,12] Structural investigations of $AgNbO_3$ have revealed that at room temperature both Ag^+ and Nb^{5+} cations experience antiparallel off-center displacements within their respective polyhedra.[13-15] However, the existence of polar regions at room temperature was ascertained by detailed diffraction studies has been reported more recently.[12,16,17] The coexistence of antiferroelectric (AFE) and FE states in $AgNbO_3$ yields a complicated sequence of electric field-induced events, as observed in the current-polarization-electric field hysteresis loops previously reported.[12]

It was found that bismuth niobate, $BiNb_3O_9,$ crystalizes as an A-site deficient metastable perovskite super-cell structure (*i.e*., $Bi_{1/3}NbO_3$).[18] Additionally, the ionic radius Bi^{3+} is smaller than that of Ag^+ ($r = 1.17$ and 1.28 Å, respectively for the ions in eight coordinate geometry),[19] which is beneficial for reducing the perovskite tolerance factor and the promotion of antiferroelectricity.[20] Thus, bismuth might be

expected to show some solubility in the silver niobate structure and this could be used to improve the energy storage characteristics of $AgNbO_3$. In the present work we report the structure and dielectric properties of ceramics in the $AgNbO_3$-$Bi_{1/3}NbO_3$ (*i.e.*, $Ag_{1-3x}Bi_xNbO_3$) pseudo-binary solid solution. Bismuth substitution in this system is shown to enhance energy density and efficiency.

2. Experimental

Polycrystalline ceramic samples of $Ag_{1-3x}Bi_xNbO_3$ (ABN*x*, $0.005 \leq x \leq 0.040$) were synthesized by a conventional solid-state process. All starting materials were purchased from Sinopharm Chemical Reagent Co. Ltd., China. Stoichiometric amounts of Ag_2O (99.7%), Nb_2O_5 (99.99%) and Bi_2O_3 (99.9%) were ground in ethanol for 12 hours using a planetary ball mill (QM-3SP4, Nanjing University Instrument, China). After drying, the mixtures were placed into alumina porcelain boats and heated to 800 °C, at a heating rate of 5 °C min^{-1}, in a tube furnace (GLS-1600X, Hefei Kejing, China) and calcined at this temperature for 4 h, in flowing oxygen at a rate of 500 cm^3 min^{-1}. The calcined powders were re-ground in the ball mill for 4 h in ethanol. After drying, the powders were mixed with 5 wt% polyvinyl alcohol (PVA) solution and pressed into pellets with a diameter of 15 mm and thickness of 1~2 mm under 400 MPa uniaxial pressure. The pellets were heated at a rate of 5 °C min^{-1} to 600 °C and held at this temperature for 2 h to burn off the PVA. The samples were subsequently sintered at temperatures between 1060 and 1090 °C in oxygen at a flow rate of 500 cm^3 min^{-1} for 6 h, followed by cooling to ambient temperature, at a rate 5 °C min^{-1}. The color of the resulting ceramic pellets was bright yellow.

For crystal structure characterization, the pellets were ground to ensure that the structure was representative of the bulk ceramic. Samples were then manually crushed into fine powders. X-ray powder diffraction (XRD) data were collected on a PANalytical X'Pert Pro diffractometer (PANalytical, Cambridge, UK), fitted with an X'Celerator detector, in θ/θ geometry using Ni-filtered Cu-Kα radiation (λ =1.5418

Å), over the 2θ range 10 to 100° in steps of 0.0167°, with an effective count time of 300 s per step.

For electrical characterization, silver electrodes were painted on parallel faces of the ceramic disks. Temperature-dependent dielectric data were collected by measuring the capacitance and loss at different frequencies on heating, using an LCR meter (Agilent E4980A) connected to a computer-controlled temperature chamber. The d.c. field dependence of dielectric permittivity was measured using an LCR meter (TH 2828S, Changzhou, China) connected to a high voltage source (Keithley 6517). To measure electric displacement - electric field (*D-E*) and current - electric field (*I-E*) hysteresis loops, gold electrodes were sputtered on the two main surfaces of polished specimens (with thickness of *ca.* 0.3 mm). The measurement was carried out using a ferroelectric measurement system (NPL, Teddington, UK).[21] The hysteresis loops were measured separately at low and high electrical fields to investigate the sequence of electric field-induced transitions. The differential permittivity (*dD/dE*) was calculated from the *D-E* loops.

3. Results and Discussion

The fitted XRD patterns of the studied ABN*x* compositions are given as supplementary information in Fig. S1, with the crystal and refinement parameters summarized in Table S1. The fits confirm that all samples were single phase, within the limits of the technique, with an average *Pbcm* structure, as seen in the unsubstituted parent phase AgNbO$_3$.[12,13-15] The compositional variations of lattice parameters and cell volume are shown in Fig. 1. The lattice parameters *a*, *b* and the unit cell volume generally decrease with increasing *x*-value, while the *c*-axis parameter shows a general increase with increasing level of substitution, consistent with solid solution formation. The *b/a* cell parameter ratio shows two approximately linear regions, with a step between *x* = 0.015 and 0.020. This is reflected in the volume plot, which switches from a linear to a curved region at *x* = 0.020. The volume decrease is consistent with substitution of Ag$^+$ by Bi^{3+} cations with smaller

5

ionic radius. However, at these levels of substitution, the results cannot easily distinguish between the three main possible solid solution mechanisms:
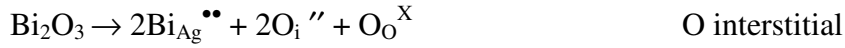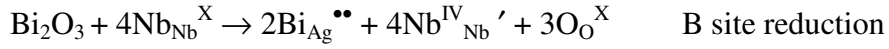
$$Bi_2O_3 \rightarrow 2Bi_{Ag}^{\bullet\bullet} + 4V_{Ag}{}' + 3O_O^X \qquad \text{A site cation vacancy}$$

$$Bi_2O_3 + 4Nb_{Nb}^X \rightarrow 2Bi_{Ag}^{\bullet\bullet} + 4Nb^{IV}{}_{Nb}{}' + 3O_O^X \qquad \text{B site reduction}$$

$$Bi_2O_3 \rightarrow 2Bi_{Ag}^{\bullet\bullet} + 2O_i{}'' + O_O^X \qquad \text{O interstitial}$$

Fig. 2 shows the temperature dependence of the real and imaginary components of dielectric permittivity at 1 MHz. A number of dielectric anomalies are observed in the plots for ABN005 and can be attributed to a series of phase transitions similar to those observed in AgNbO₃.[11,12] The dielectric anomalies at *ca.* 50 °C and *ca.* 260 °C, are associated with transitions that maintain the $(a^-,b^-,c^+)/(a^-,b^-,c^-)$ octahedral tilting system, *viz.*: $M_1 \leftrightarrow M_2$ and $M_2 \leftrightarrow M_3$ transitions, respectively.[14,15] However, to date the structural details of these transitions are unclear. An extra anomaly was observed in the imaginary part of the dielectric permittivity (ε_r'') at *ca.* 170 °C, which is assigned to the freezing temperature (T_f), where the antipolar dipoles become frozen as the cations order.[15,22] The sharp maximum near 350 °C and the shoulder near 400 °C are attributed to phase transitions between phases with different octahedral tilting systems, *i.e.* orthorhombic *Pbcm* $((a^-,b^-,c^+)/(a^-,b^-,c^-)) \leftrightarrow$ orthorhombic *Cmcm* $(a^0,b^-,c^+) \leftrightarrow$ tetragonal *P4/mbm* (a^0,b^0,c^+) transitions, respectively.[14] The temperatures corresponding to all these dielectric peaks are frequency independent (Fig. S2). As shown in Fig. 2, with increasing *x*, all the dielectric anomalies shift to lower temperature. The dielectric anomalies corresponding to the $M_1 \leftrightarrow M_2$ transition and the T_f are shifted below room temperature at compositions $x \geq 0.010$ and $x > 0.020$, respectively.

Fig. 3 shows the variation of dielectric permittivity of ABN*x* ceramics under d.c. field. The dielectric permittivity of ABN*x* ceramics decreases with increasing d.c. field, as the system becomes less polarizable when it approaches saturation. For the *x*

= 0.005 composition, there is a clear drop in dielectric permittivity at zero field, compared to the initial state, after initial application and removal of the d.c. field. This can be attributed to a decrease in FE domain wall density, in agreement with previous studies.[23] In contrast, at higher x-value compositions, there is no clear drop of permittivity after application and removal of the d.c. field, which suggests that these compositions have less polarizable structures. The d.c. field-induced variations of dielectric permittivity decrease with increasing x-value, consistent with the ceramics progressively evolving towards an antiferroelectric state. The ABN040 ceramic exhibits very stable dielectric permittivity under d.c. field compared to the other compositions, consistent with the structure being antiferroelectric. Similar results are seen in antiferroelectric $PbZrO_3$, which also shows no variation in dielectric permittivity under a bias field, when this field is lower than the critical field required to induce the AFE-FE transformation.[24]

Fig. 4 shows the D-E and I-E loops of ABNx ceramics up to 6 MV m^{-1}. The loops relative to the ABN005 ceramic (Fig. 4a) can be interpreted based on the idea that the local polar regions and FE domains that might be initially present in $AgNbO_3$,[12,25,26] are slightly diminished by low levels of bismuth substitution. The I-E loop of $AgNbO_3$ in fact showed two peaks in the loading branch (indicated by $E_1 = 0.3$ MV m^{-1} and $E_2 = 2.5$ MV m^{-1} in Ref.12), which can be attributed to complicated domain switching events relative to the local polar regions. Whilst these local polar regions appear to be ferroelectric, the possibility of them being ferrielectric in nature cannot be excluded.[16] In ABN005, the current peaks are not clearly visible, in agreement with the view that bismuth addition hinders the presence of polar region (or reduces their polarity). However, a closer look at Fig. 4a reveals the presence of a rather smeared and broad current bump (roughly 2 MV m^{-1}, ie., E_2). This may correspond to a local electric field-induced transition, which would expand the polar regions (or increase their polarity). The current peaks E_1, near zero field could therefore contain the contribution of the reversed transition occurring during unloading, and the contribution of the domain switching event that in $AgNbO_3$ has been associated with the peak E_1 (during loading), which here might be responsible for the tail of the

7

current peak appearing in the loading branch. With increasing x-value, the E_2 peak in ABNx ceramics becomes weaker and broader, when T_f is below room temperature. The composition ABN040 shows linear dielectric behavior with no presence of domain switching peaks in the I-E loop (Fig. 4b), which further supports the proposition that the structure of this composition is antiferroelectric. This is consistent with the observation that the E_2 peak completely disappears when T_f is below room temperature.

Fig. 5 shows the high field D-E loops and dD/dE-E loops of the studied ABNx ceramics. As the x-value increases, the field-induced ferroelectric polarization decreases (Fig. 5a), with the maximum electric displacement, D_m, decreasing from 0.40 C m^{-2} to 0.23 C m^{-2} at the highest applied field, while the remnant electric displacement (D_r) becomes almost zero at $x = 0.030$. At $x = 0.040$, a linear-like D-E hysteresis is observed. In Fig. 5b, $\pm E_F$ represents the electric forward field required to transform the initial structures to a ferroelectric state, while the backward field required to reverse the transition is denoted as $\pm E_B$. All ceramics show double D-E loops and four peaks in their dD/dE-E loops. Additionally, two small peaks (denoted as $\pm E_U$) are observed in compositions with $x < 0.020$. Analogous peaks were observed in ferroelectric loops for pure AgNbO$_3$ ceramic,[10] which were attributed to a polarizable ferrielectric-like structure below T_f. In contrast, there are no clear $\pm E_U$ peaks in the dD/dE-E loops of ABNx ceramics with $x \geq 0.020$ (Fig. 4b); this supports the idea that the structure above T_f is non-polarizable antiferroelectric (see Fig. 2). Additionally, the results suggest that with increasing x-value, the local polar ferroelectric or ferrielectric behavior is suppressed and that the AFE structure becomes more favored at room temperature, with a reduced ability to be polarized under the application of an electric field.

Fig. 6 shows the compositional variation of E_F and E_B. Both E_F and E_B shift to higher field with increasing x-value. This increase can lead to higher energy density. Moreover, the difference (ΔE) between E_F and E_B decreases with increasing x-value, which can result in improved energy storage efficiency. The schematic energy storage process of an ideal antiferroelectric capacitor is shown in Fig. 7a, where recoverable

energy density (W_{rec}) and energy loss (W_{loss}) are represented by the red and black areas, respectively. The energy efficiency (η) can be calculated as:

$$\eta = W_{rec.}/[W_{loss} + W_{rec.}]$$

The calculated energy storage density and efficiency of the studied ABNx ceramics is shown in Fig. 7b. The maximum recoverable energy density $W_{rec.}$ (3 J cm^{-3}) was achieved in the ABN010 composition, as a result of the favorable balance between D_m (which decreases with increasing x-value) and the increased electric field required to induce the reversible phase transitions (which increases with increasing x-value). The optimal energy storage performance (with a high recoverable energy density W_{rec} of 2.6 J cm^{-3} and high energy efficiency of 0.86) was obtained in the ABN030 ceramic. The ceramics ABN010 and ABN030 show higher recoverable energy density W_{rec} than any other known lead free ceramics, as shown in Fig. 7c, which depicts the relationship between W_{rec} and applied field E, for recently developed lead-free dielectric materials. The AgNbO$_3$-based ceramics typically show high W_{rec} values of 2~3 J cm^{-3} at low applied fields of around 200 kV cm^{-1}. Among ABN ceramics, ABN030 offers the highest energy efficiency, η, as shown in Fig.7b. The main benefit of bismuth substitution in the ABNx ceramics compared to the unsubstituted parent material is the significant increase in the efficiency, which is double that of pure AgNbO$_3$ (Fig. 7b). The efficiency of ABN030 is amongst the highest values found in lead-free ceramics (Fig. 7d).

4. Conclusions

Ceramics of composition Ag$_{1-3x}$Bi$_x$NbO$_3$ (0.005 $\leq$ x $\leq$ 0.040) were successfully prepared by solid state methods. The effect of bismuth substitution is to suppress the formation of local polar regions, to induce antiferroelectric order and to increase stability under electric field loading. Increasing levels of bismuth substitution also leads to a progressive decrease of the temperatures associated with the M$_1$ to M$_2$ and

9

M_2 to M_3 phase transitions and of the freezing temperature T_f. Above T_f, the structure of the M_2 phase is AFE, while below T_f the structure contains local polar regions and is polarizable. The hysteresis loop measurements indicated that the domain switching events found in the M_1 phase of $AgNbO_3$ are suppressed for low substitution levels. The presence of electric field induced antiferroelectric to ferroelectric transitions is increasingly hindered with increasing bismuth content. The difference between the M_1 and the M_2 phases below T_f is that while the M_1 phase has locally stabilized ferroelectric domain structure, the M_2 phase only exhibits local polar regions. The difference between forward and back field decreases with increasing x-value leading to higher energy efficiency compared to unsubstituted $AgNbO_3$. An optimal energy storage performance with a high energy storage density of 2.6 J cm^{-3} and high energy efficiency of 0.86 was achieved in the composition $Ag_{0.91}Bi_{0.03}NbO_3$.

Acknowledgements

References

1. Q. Li, L. Chen, M. R. Gadinski, S. Zhang, G. Zhang, H. Li, A. Haque, L. Q. Chen, T. Jackson and Q. Wang, *Nature,* 2015, **523**, 576

2. Z. Dang, J. Yuan, S. Yao and R. Liao, *Adv. Mater.*, 2013, **25**,6334

3. L. Jin, F. Li and S. Zhang, *J.Am.Ceram.Soc.*2014, **97**, 1.

4. Y. Zhao, X. Hao, Q. Zhang, *ACS Appl. Mater. Interfaces*, 2014, **6**, 11633−11639.

5. B. Peng, Qi. Zhang, X. Li, T. Sun, H. Fan, S. Ke, M. Ye, Y. Wang, W. Lu, H. Niu, X. Zeng and

H. Huang, *ACS Appl. Mater. Interfaces,* 2015, **7**, 13512.

6. L. Jin, R. Huo, R. Guo, F. Li, D. Wang,Y. Tian, Q. Hu, X. Wei, Z. He, Y. Yan, and G. Liu, *ACS Appl. Mater. Interfaces*, 2016, **8**, 31109-31119.

7. Y. Tian, X. Chao, L.Jin, L.Wei, P. Liang, and Z. Yang, *Appl. Phys. Lett.*, 2014, **104**, 112901.

8. X. Wei, H. Yan, T. Wang, Q. Hu, G. Viola, S. Grasso, Q. Jiang, L. Jin, Z. Xu and M. J. Reece, *J. Appl. Phys.,* 2013, **113**, 024103.

9. F. Li, J. Zhai, B. Shen, X. Liu, K. Yang, Y. Zhang, P. Li, B. Liu, and H. Zeng, *J. Appl. Phys*. 2017. **121**, 054103.

10. L. Zhao, Q. Liu, S. Zhang and J. Li, *J. Mater. Chem. C*, 2016, **4**, 8380.

11. D. Fu, M. Endo, H. Taniguchi, T. Taniyama and M. Itoh, *Appl. Phys. Lett.,* 2007, **90**, 252907.

12. Y. Tian, L. Jin, H. Zhang, Z. Xu, X.Wei, E. D. Politova, S. Yu. Stefanovich, Nadezda V. Tarakina, I.Abrahams and H.Yan , *J. Mater. Chem. A*, 2016,**4**, 17279-17287

13. J. Fábry, Z. Zikmund, A. Kania and V. Petrícek, *Acta Crystallogr. C*, 2000, 56, 916.

14. P. Sciau, A. Kania, B. Dkhil, E. Suard and A. Ratuszna, *J. Phys.: Condens. Matter*, 2004, **16**, 2795.

15. I. Levin, V. Krayzman, J. C. Woicik, J. Karapetrova, T. Proffen, M. G. Tucker and I. M. Reaney, *Phys. Rev. B: Condens. Matter Mater. Phys.*, 2009, **79**, 104113.

16. M. Yashima, S. Matsuyama, R. Sano, M. Itoh, K. Tsuda and D. Fu, *Chem. Mater,* 2011, **23**, 1643.

17. H. Moriwake, A. Konishi, T. Ogawa, C. A. J. Fisher, A. Kuwabara and D. Fu, *J. Appl. Phys.*, 2016, **119**, 064102.

18. W. G. Mumme, I. E. Grey, B. Edwards, C. Turner, J. Nino and T. A. Vanderah, *J. Soli. Stat. Chem.*2013, **200**, 323–327.

19. R. D. Shannon, *Acta Cryst.* 1976, **A32**, 751.

20. H. Shimizu, H. Guo, S. E. Reyes-Lillo, Y. Mizuno, Karin M. Rabe and C. A. Randall, D*alton Trans.*, 2015, **44**, 10763.

21. H. Yan, F. Inam, Giuseppe, Viola, H. Ning, H. Zhang, Q. Jiang, T. Zeng, Z. Gao and M. J Reece, *J. Adv. Dielectr.* 2011, 1, 107118

22. A. Kania and J. Kwapuliński, *J. Phys.: Condens. Matter,* 1999**, 11**, 8933.

23. Y. Masuda, *Jpn. J. Appl. Phys*. 1994, **33**, 5549.

24. G. Shirane, E. Sawaguchi and Y. Takagi, *Phys Review*, 1951, **84**, 476.

25. A. Kania, K. Roleder, and M. Łukaszewski, *Ferroelectrics*, 1984, **52**, 265.

26. A. Kania, K. Roleder, *Ferroelectric Lett.*,1984, **2**, 51.

27. Q. Hu, L. Jin, T. Wang, C. Li, Z. Xing and X. Wei, *J. Alloys Compd.*, 2015, **640**, 416.

28. T. Wang, L. Jin, C. Li, Q. Hu and X. Wei, *J. Am. Ceram. Soc.*,2015, **98**, 559.

29. Z. Shen, X. Wang, B. Luo and L. Li, *J. Mater. Chem. A*, 2015, **3**,18146.

30. Z. Song, H. Liu, S. Zhang, Z. Wang, Y. Shi, H. Hao, M. Cao, Z. Yao and Z. Yu, *J. Eur. Ceram. Soc.*, 2014, **34**, 1209.

31. J. Ding, Y. Liu, Y. Lu, H. Qian, H. Gao, H. Chen and C. Ma, *Mater. Lett.*, 2014, **114**, 107.

32. L. Luo, B. Wang, X. Jiang and W. Li, *J. Mater. Sci.*, 2014, **49**,1659.

33. Q. Xu, T. Lia, H. Hao, S. Zhang, Z. Wang, M. Cao, Z. Yao and H. Liu, *J. Eur. Ceram. Soc.*, 2014, **34,** 1209.

34. J. Ye, Y. Liu, Y. Lu, J. Ding, C. Ma, H. Qian and Z. Yu, *J. Mater. Sci.: Mater. Electron.*, 2014, **25**, 4632.

35. H. Borkar, V. N. Singh, B. P. Singh, M. Tomar, V. Gupta and A. Kumar, *RSC Adv.*, 2014, **4**, 22840.

36. B. Wang, L. Luo, X. Jiang, W. Li and H. Chen, *J. Alloys Compd.*, 2014, **585**, 14–18.

37. B. Qu, H. Du and Z. Yang, *J. Mater. Chem. C*, 2016, **4**, 1795.

38. A. C. Larson and R. B. Von Dreele, *Los Alamos National Laboratory Report*, *No. LAUR-86–748,* 1987.
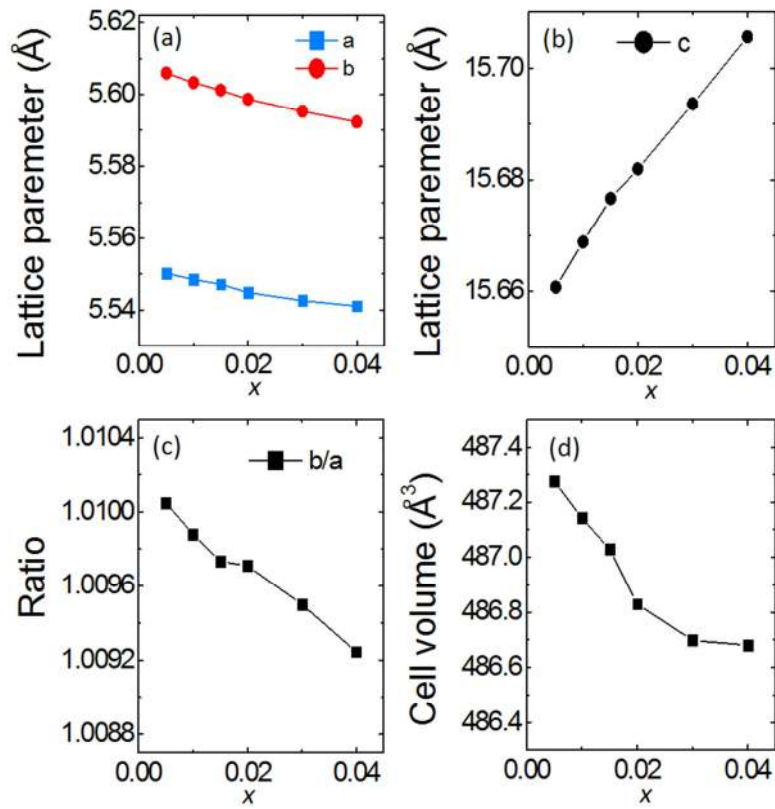
Figure and Figure Captions

Abstract Graphic
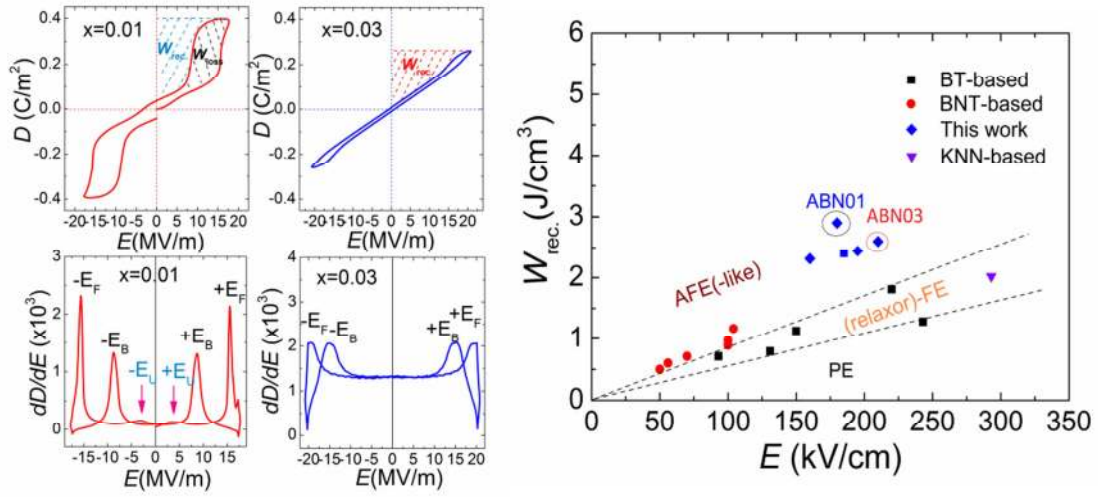
Fig.1.   Compositional variation of (a) *a* and *b* lattice parameters (b) *c* lattice
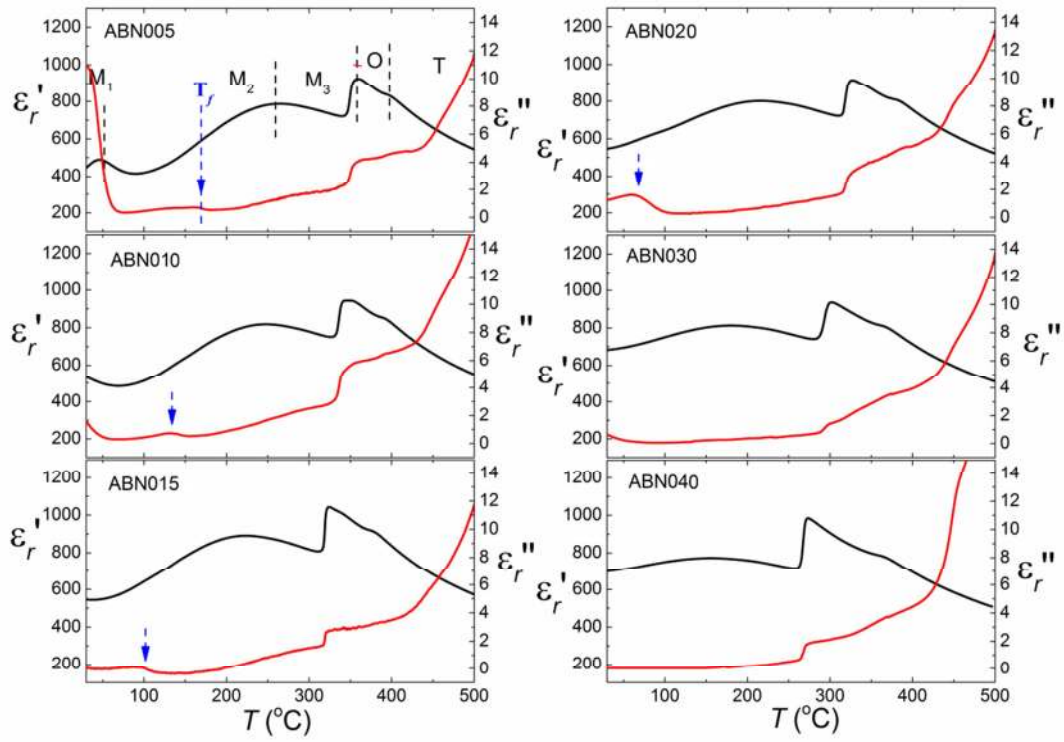parameter (c) *b*/*a* lattice parameter ratio and (d) unit cell volume in ABN*x* ceramics.

Fig. 2. Thermal dependence on heating of real (ε_r') and imaginary (ε_r'') parts of relative permittivity in ABNx ceramics at 1 MHz.
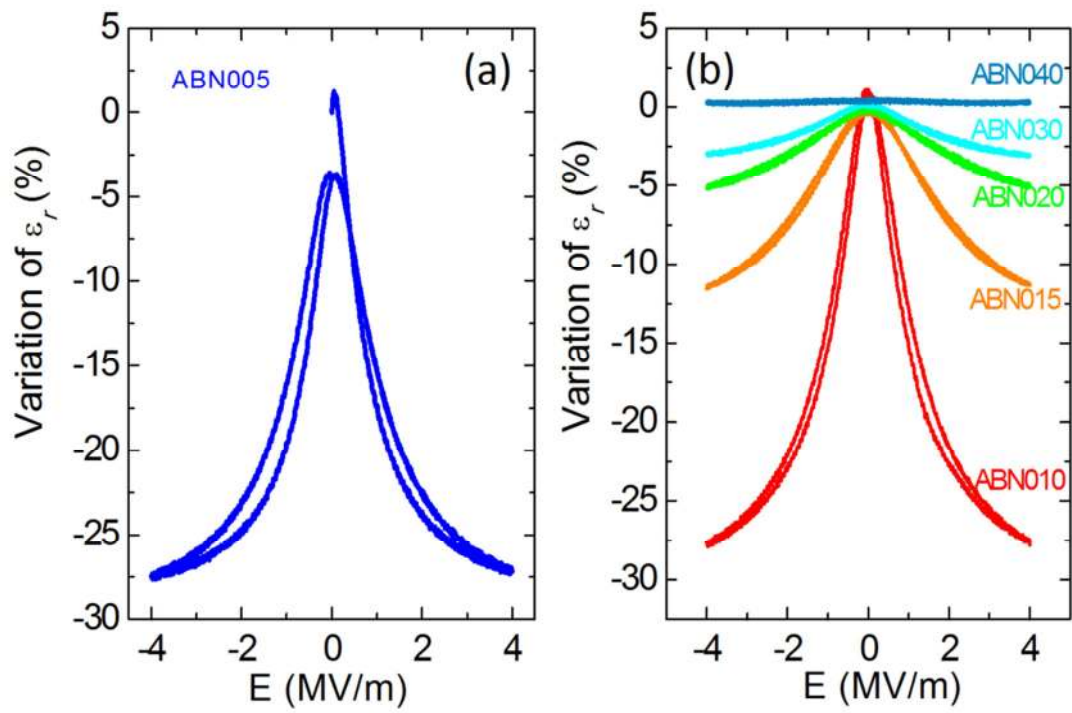
Fig. 3. Percentage variation in relative permittivity (ε_r) at low field in ABNx ceramics measured at 1 kHz.
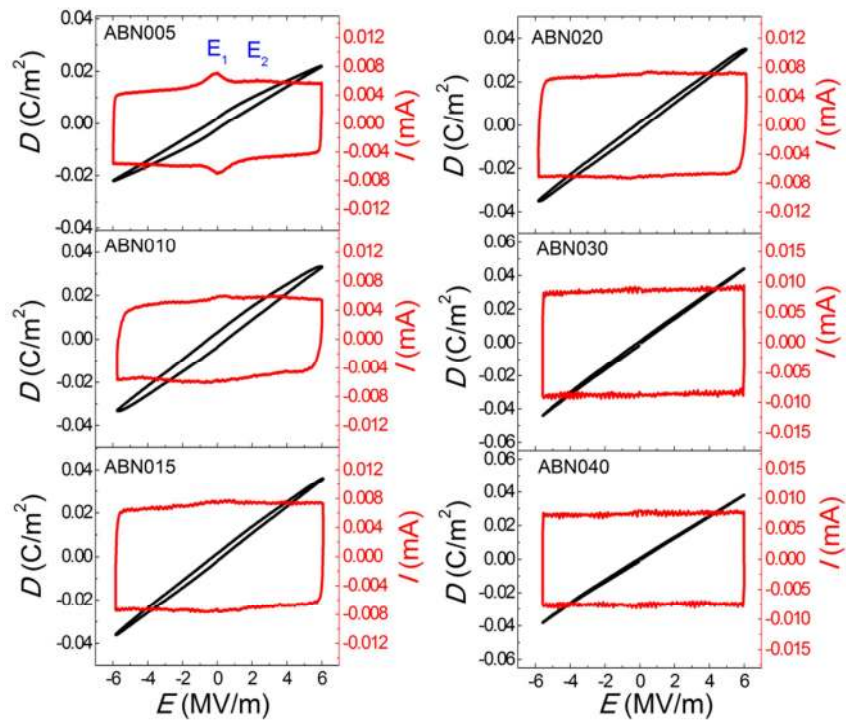
Fig. 4. Low field ferroelectric *D-E* and *I-E* loops measured at 10 Hz for ABNx ceramics.
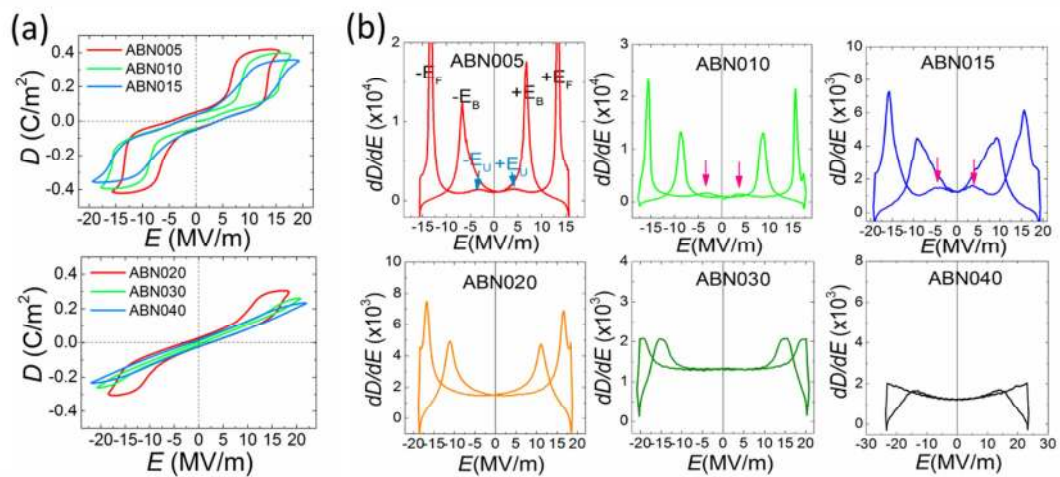
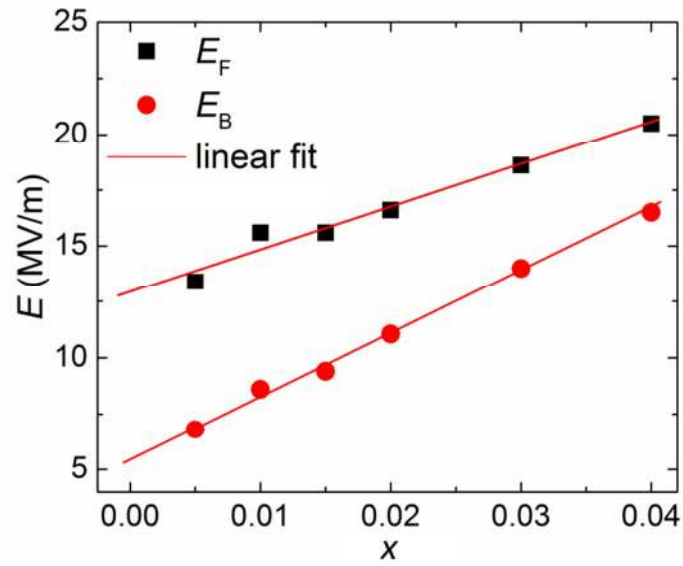Fig. 5. High field ferroelectric (a) *D-E* and (b) *dD/dE-E* loops of ABN*x* ceramics measured at 10Hz.

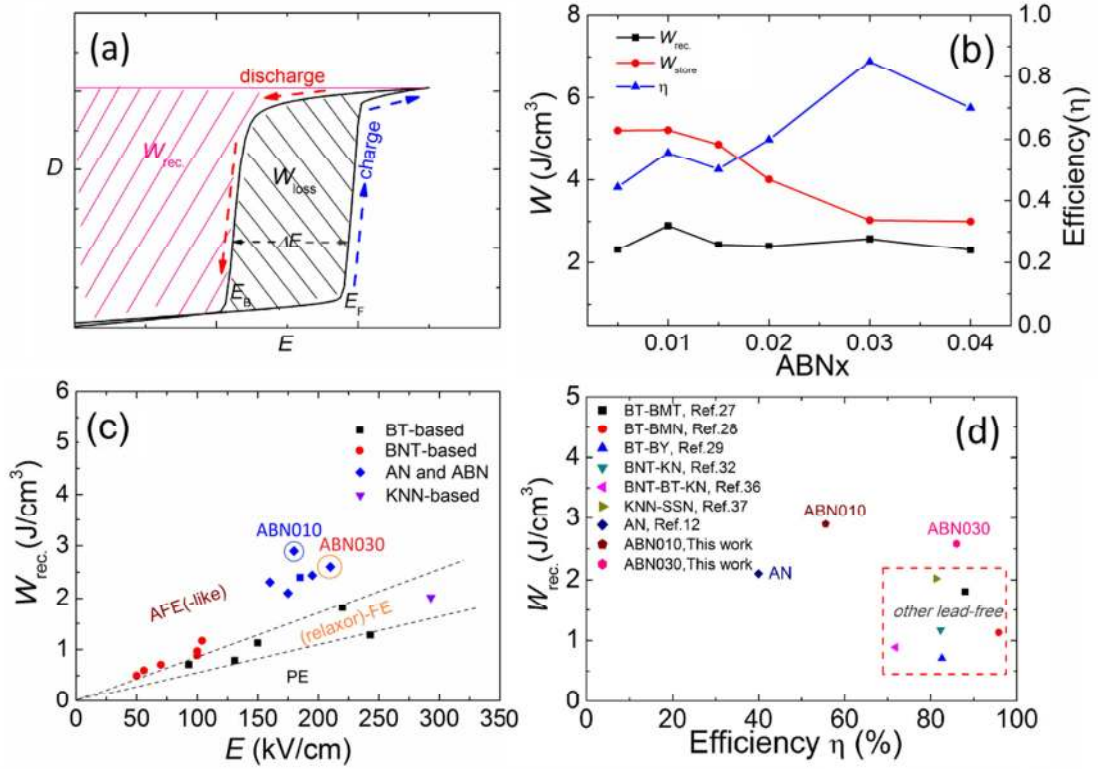Fig. 6. Compositional variation of forward (E_F) and backward (E_B) field in ABNx ceramics.

Fig. 7. (a) Schematic energy storage process for an ideal antiferroelectric capacitor; (b) energy storage density (W) and efficiency (η) of ABNx ceramics; (c) comparison of recoverable energy density (W_{rec}) in ABN010 and ABN030 with that in other lead-free ceramic systems: BT (BaTiO$_3$-based, Hu et al,[27] Wang et al,[28] Shen et al,[29] and Song et al,[30]); BNT (Bi$_{0.5}$Na$_{0.5}$TiO$_3$-based, Ding et al,[31] Luo et al,[32] Xu et al,[33] Ye et al,[34] Borkar et al, [35] and Wang et al,[36]); KNN (K$_{0.5}$Na$_{0.5}$NbO$_3$-based. Qu et al,[37]) and (d) W_{rec} versus η for ABN030 ceramic compared to other lead-free ceramic systems (Tian et al,[12] Hu et al,[27] Wang et al,[28] Shen et al,[29] Luo et al,[32] Wang et al,[36] Qu et al,[37]).
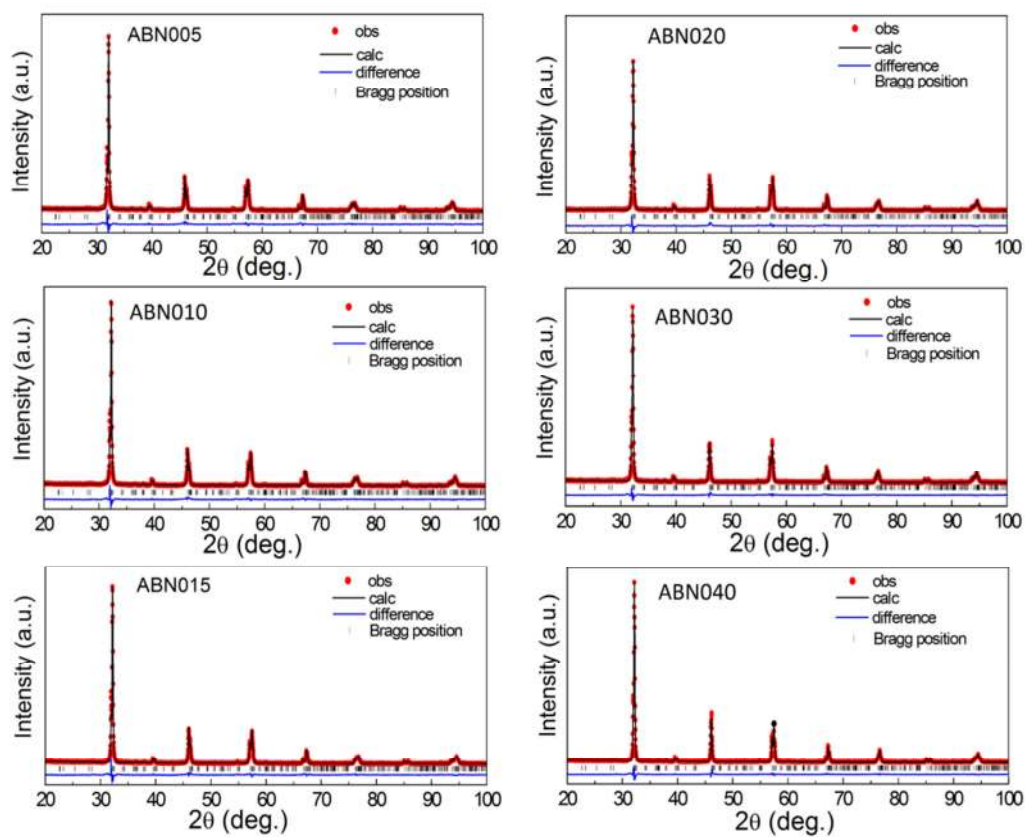
Supplementary Information

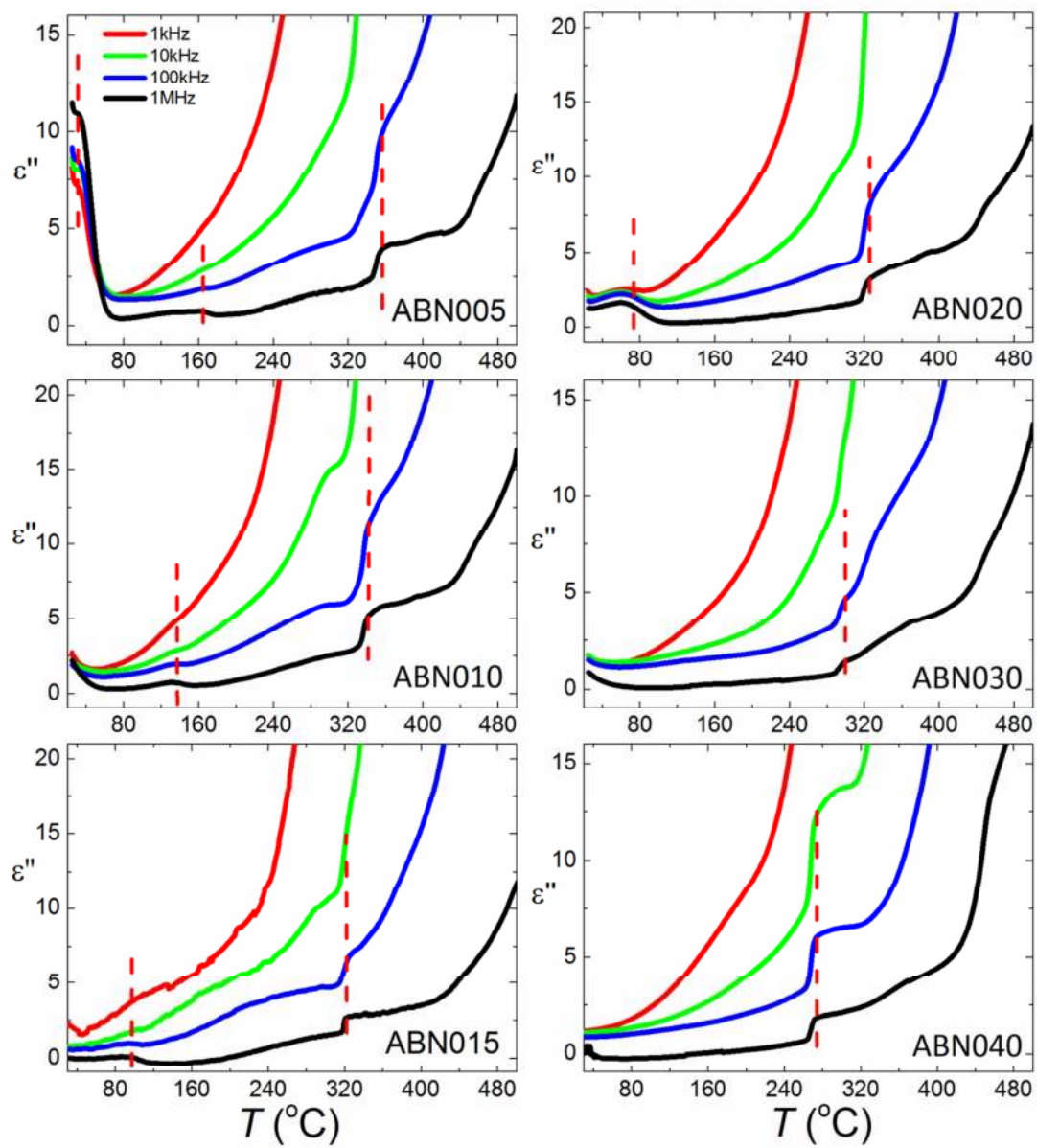Fig. S1. Fitted X-ray diffraction profiles for crushed ABN*x* ceramic powders.

Fig. S2. Temperature dependence on heating of imaginary (ε'') part of dielectric permittivity in ABNx ceramics.

Table S1: Crystal and Refinement parameters for $Ag_{1-3x}Bi_xNbO_3$. Estimated standard deviations are given in parentheses.

Chemical formula	$Ag_{0.985}Bi_{0.005}NbO_3$	$Ag_{0.97}Bi_{0.01}NbO_3$	$Ag_{0.955}Bi_{0.015}NbO_3$	$Ag_{0.94}Bi_{0.02}NbO_3$	$Ag_{0.91}Bi_{0.03}NbO_3$	$Ag_{0.88}Bi_{0.04}NbO_3$
Formula weight	248.20 g mol^{-1}	257.62 g mol^{-1}	247.05 g mol^{-1}	246.48 g mol^{-1}	245.33 g mol^{-1}	244.19 g mol^{-1}
Crystal system	Orthorhombic	Orthorhombic	Orthorhombic	Orthorhombic	Orthorhombic	Orthorhombic
Space group	*Pbcm*	*Pbcm*	*Pbcm*	*Pbcm*	*Pbcm*	*Pbcm*
Unit cell dimensions	a = 5.5502(2) Å	a = 5.5484(2) Å	a = 5.5471(2) Å	a = 5.5448(2) Å	a = 5.5426(1) Å	a = 5.5411(1) Å
	b = 5.6059(2) Å	b = 5.6033(2) Å	b = 5.6011(2) Å	b = 5.5986(2) Å	b = 5.5952(1) Å	b = 5.5923(1) Å
	c = 15.6607(5) Å	c = 15.6688(5) Å	c = 15.6765(5) Å	c = 15.6819(5) Å	c = 15.6935(4) Å	c = 15.7055(3) Å
Volume	487.27(3) Å^3	487.14(3) Å^3	487.08(3) Å^3	486.83(3) Å^3	486.69(2) Å^3	486.68(2) Å^3
Z	8	8	8	8	8	8
Density(calculated)	6.766 g cm^{-3}	6.753 g cm^{-3}	6.738 g cm^{-3}	6.724 g cm^{-3}	6.696 g cm^{-3}	6.665 g cm^{-3}
R-factors[a]	R_{wp} = 0.0401	R_{wp} = 0.0373	R_{wp} = 0.0409	R_{wp} = 0.0369	R_{wp} = 0.0328	R_{wp} = 0.0348
	R_p = 0.0282	R_p = 0.0256	R_p = 0.0289	R_p = 0.0263	R_p = 0.0243	R_p = 0.0251
	R_{ex} = 0.0165	R_{ex} = 0.0160	R_{ex} = 0.0166	R_{ex} = 0.0163	R_{ex} = 0.0164	R_{ex} = 0.0595
	R_F^2 = 0.1274	R_F^2 = 0.1084	R_F^2 = 0.1757	R_F^2 = 0.1208	R_F^2 = 0.1081	R_F^2 = 0.1164
Total No. of variables	27	27	27	27	27	27
No. of profile points used	3460	3460	3460	3460	3460	3460

[a] For definition of R-factors see ref.38.